Biophysical Design Space for Cellular Self-assembly and Dynamics

Sanbed Das[1], M Sreepadmanabh[2], Dikshant Parashar[1], Tapomoy Bhattacharjee[2,#], Sayantan Dutta[1,*]
[1]*Department of Chemical Enginnering, IIT Bombay, Powai, Mumbai, India*
[2]*National Centre for Biological Sciences, Tata Institute of Fundamental Research, Bangalore, India*

In natural biological systems, cells organize into tissues through interactions of several processes, including cellular signaling, collective migration, contractile activity of cytoskeletal elements and interactions with their surroundings. In recent decades, advancements in microscopy, genetic engineering, biochemistry, and computational modeling have enabled a more quantitative understanding of these processes. In this article, we present an integrated computational framework that couples various physical mechanisms such as: cell-cell adhesion , strength and persistence of cellular motility, and the background stiffness, to study how they collectively interact to determine the self-organization starting from a pseudo-random structure as well as the migration behavior. Notably, our simulations predict that motility has a two-way effect on cellular self-assembly: it promotes aggregation at moderate levels but disrupts clusters when excessively strong, yielding an optimal motility for formation of multicellular clusters. On the other hand, adhesion shows a two-stage effect: At lower value it self-assembles the structure, at higher value it compacts it. Furthermore, We experimentally demonstrate the *motility-assisted* self-aggregation of cells using cancer cells in a granular mechanical milieu. Finally we show that cell-cell adhesion and background medium tune the strength and persistence of cellular migration. Altogether, this work presents a computational framework that allows us to design phase behavior of collective of cells tuning their interaction, motility, and the background mechanics.

I. INTRODUCTION

Cells, fundamental building blocks of life, self-assemble to spatially organized and functional structures such as organs and tissues. Self-organization of cells is a central *design* principle in numerous physiological processes, including tissue pattern formation leading to embryonic morphogenesis [1, 2], wound healing [3–5], immune response [6], and regeneration. When these *designs* fail, consequences can be severe, leading to pathological conditions such as tumor invasion [7] or fatal developmental abnormalities [8, 9]. The same organizing principles are often leveraged in generating *in vitro* assemblies of cells such as organoid [10]. A set of biophysical mechanisms interact with each other and set the *design* rules of this self-organization. Cells bind to one another through E-cadherin–mediated adhesion [11] and form multicellular clusters [12]. As they proliferate, local density increases and cells generate specific packing to accomodate each other [13, 14]. Cells migrate—sometimes directionally following a cue (taxis) [15, 16], sometimes randomly (kinesis) [17] to explore the surrounding medium. Cell-Cell communication occurs through chemical signaling as well as through forces transmitted by cytoskeletal elements such as microtubules [18] and actomyosin [19, 20]. At the same time, cells interact with the biochemical and mechanical properties of their surrounding medium and respond passively or adjust their behavior [21, 22]. Together, these mechanisms promote the spontaneous formation of organized multicellular assemblies with specific structure and function.

Active matter physics has devoted considerable effort over the last decade to modeling the self-organization and dynamics of self-propelled particles [23–25]. Unlike passive colloidal particles, whose aggregation is governed by equilibrium forces, self-propelled particles can reorganize even without attractive interactions. A key example is motility-induced phase separation, where self-propulsion alone drives the formation of dense clusters and spatially segregated domains [26, 27]. Typical ingredients used to model the self-organization of such particles include self-propulsion described as Ornstein–Uhlenbeck noise [28] or active Brownian motion [29], interparticle forces represented through Lennard-Jones (LJ) [29] or Weeks–Chandler–Anderson (WCA) [30] potentials, and alignment of propulsion directions between neighboring units captured by the Vicsek model [31]. These interactions generate a rich set of emergent behaviors, including dynamic clustering [32, 33], flocking [34–37], and swarming [38] and transitions between jammed to unjammed states [39].

Physical realizations of self-propelled interacting active matter span multiple scales, from reactive droplets [40] and biomolecular condensates at molecular dimensions [41] to insect swarms and schools of fish at population scales [42, 43]. The self-organization of cells are also examples of such system in an intermediate length-scale as cells are interacting, self-propelled active particles [44–46]. In this article, we present a computational framework that describes the self-assembly of cells using principles from soft and active matter physics. Specifically, we treat cells as soft self-propelling particles that

[1] *sayantan.dutta@iitb.ac.in
#tapa@ncbs.res.in

adhere to one another and are submerged in a viscoelastic medium represented by gels, and using this framework we demonstrate how different biophysical mechanisms interplay with each other to determine the cellular self-assembly and dynamics. Moreover, we validate some of the predictions using *in vitro* experiments involving self-aggregating cancer cells suspended in a granular microgel matrix.

II. MODEL DESCRIPTION

We employ a particle-based simulation framework to investigate the dynamics of cellular self-organization. Our model consists of two kinds of particles: cells and background particles (denoted as gels) representing a viscoelastic medium. We perform the simulations in a cubic (3D)/square (2D) box with periodic boundary conditions [Fig. 1 (a),(b)]. The equation of motion for a particle i follows overdamped Langevin dynamics:

$$\eta \frac{\partial \vec{r_i}}{\partial t} = \sum_{i \neq j} (\vec{F^{\mathrm{c}}_{ij}} + \vec{F^{\mathrm{ad}}_{ij}}) + \vec{F^{\mathrm{A}}_i}, \tag{1}$$

where, η is the coefficient of viscous drag, $\vec{F^{\mathrm{c}}_{ij}}$, and $\vec{F^{\mathrm{ad}}_{ij}}$ represent the contact and adhesive force from all other particles j, and $\vec{F}^{\mathrm{A}}$ represents the active force resulting into the motility.

The pairwise interaction forces consist of the contact force ($\vec{F^{\mathrm{c}}_{ij}}$) and the adhesion force($\vec{F^{\mathrm{ad}}_{ij}}$). Hertz force [47] is often used to describe the contact interaction between soft particles specifically for microgels and cells [48, 49] and we adapt that to describe the contact interaction [Fig. 1(c)]:

$$\vec{F^{\mathrm{c}}_{ij}} = \begin{cases} \frac{4E^*_{ij}}{3}(\sigma - r_{ij})^{1.5}\sqrt{\frac{\sigma}{2}}\frac{\vec{r_{ij}}}{|r_{ij}|}, & r_{ij} < \sigma \\ 0, & \text{otherwise} \end{cases} \tag{2}$$

where, $E^*_{ij} = \left[\frac{1-\nu_i^2}{E_i} + \frac{1-\nu_j^2}{E_j}\right]^{-1}$ [50]. E_i, and E_j are the Young's moduli and ν_i, and ν_j are the Poisson's ratio of the particles i and j. All particles have the same diameter σ, and $\vec{r}_{ij}$ is the center-to-center separation vector. Equation 2 defines a soft repulsive force that acts only when particles overlap.

Next, we non-dimensionalize the length by the diameter of the particle σ and time by $\tau = 3\eta/4E^*_{cc}\sigma$, the viscoelastic relaxation timescale associated with the elastic modulus of the cells and viscosity of the background medium. The non-dimensional equation of motion is:

$$\frac{\partial \vec{\hat{r}_i}}{\partial \hat{t}} = \sum_{i \neq j} \vec{\hat{F}^{\mathrm{c}}_{ij}} + \vec{\hat{F}^{\mathrm{ad}}_{ij}} + \vec{\hat{F}^{\mathrm{A}}_i}, \tag{3}$$

where, $\vec{\hat{r}_i} = \vec{r}_i/\sigma$ and $\hat{t} = t/\tau$. As a result, the non-dimensional forces are normalized by a factor of $\frac{\tau}{\eta\sigma}$. Specifically, the non-dimensional contact force reads as:

$$\vec{\hat{F}^{\mathrm{c}}_{ij}} = \begin{cases} 0.5\beta_{ij}(1-\hat{r}_{ij})^{1.5}\frac{\vec{\hat{r}}_{ij}}{|\hat{r}_{ij}|}, & \hat{r}_{ij} < 1 \\ 0, & \text{otherwise} \end{cases} \tag{4}$$

where, $\beta_{ij} = 1$ for cell-cell contact, $\beta_{ij} = \frac{E_g}{E_c}$ gel-gel contact and $\beta_{ij} = [\frac{1}{2}\left(1 + \frac{E_c}{E_g}\right)]^{-1}$ for cell-gel contact. We assume the Poisson's ratio to be same for all the particles.

Cell-cell adhesions are often represented by short-range attraction force similar to a Lennard-Jones interaction with a finite-cutoff [2]. We specifically use a V-shaped force that acts only between pairs of cells[Fig. 1(c)]:

$$\vec{\hat{F}^{\mathrm{ad}}_{ij}} = \begin{cases} -\hat{\epsilon}\frac{(\hat{r}_{ij}-1)}{\delta}\frac{\vec{\hat{r}}_{ij}}{|\hat{r}_{ij}|}, & 1 < \hat{r}_{ij} \leq 1+\delta \\ -\hat{\epsilon} + \hat{\epsilon}\frac{(\hat{r}_{ij}-\delta-1)}{\delta}\frac{\vec{\hat{r}}_{ij}}{|\hat{r}_{ij}|}, & 1+\delta \leq \hat{r}_{ij} \leq 1+2\delta \\ 0, & \text{otherwise} \end{cases} \tag{5}$$

where, $\hat{\epsilon}$ represents the strength of adhesion, and δ represents the half-width of the range of attractive force.

The active force in our model represents cellular motility and is inspired from the Ornstein-Uhlenbeck process [51, 52]. Active force on cell i evolves as,

$$d\vec{\hat{F}^{\mathrm{A}}_i} = -\hat{k}_a \vec{\hat{F}^{\mathrm{A}}_i} d\hat{t} + \hat{\Gamma} d\vec{W}_{\hat{t}}, \tag{6}$$

where, $1/\hat{k}_a$ represents the timescale of persistence of the cellular motion, and $d\vec{W}_{\hat{t}}$ represents a Gaussian white

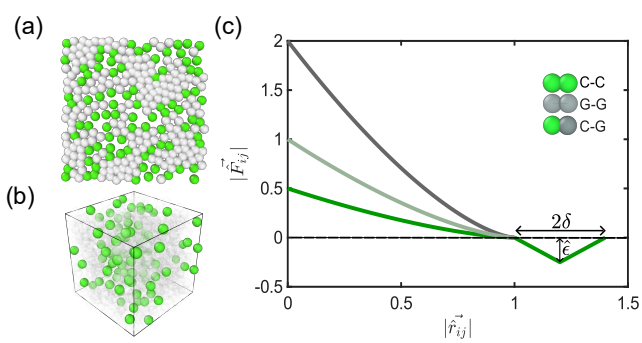

FIG. 1. Simulation snapshots from (a) two and (b) three dimensional simulation boxes respectively. Green particles denote cells and gray particles denote background (gel) particles. Gel particles are made transparent in the 3D simulation box for better visibility of cells. (c) The inter-particle interaction forces $|\vec{\hat{F}_{ij}}|$ as a function of the radial center-to-center distance $|\vec{\hat{r}_{ij}}|$. The green, light-gray, and dark-gray curves represent cell-cell, cell-gel and gel-gel interactions.

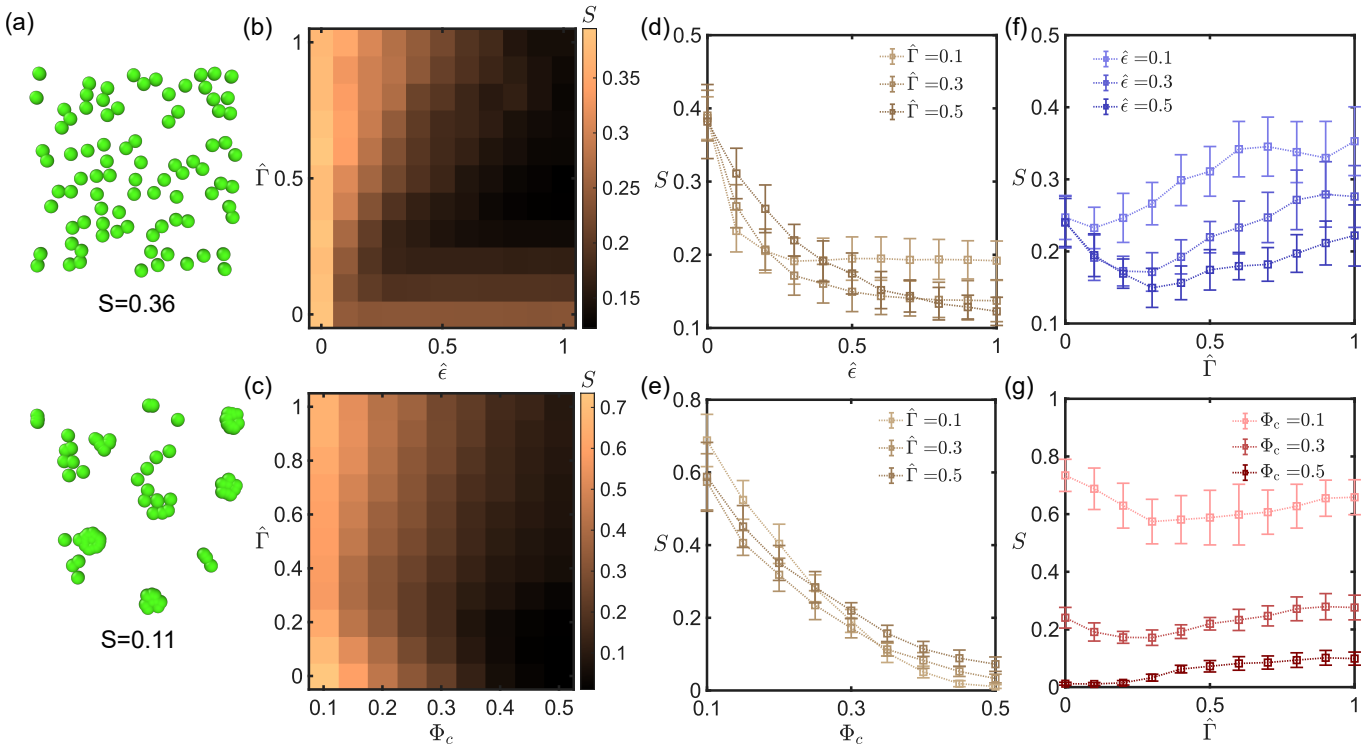

FIG. 2. (a) Order parameter S quantifies the degree of self-assembly. Two snapshots in the left represents structures with $S = 0.36$ (top), and 0.11 (bottom) respectively. Green particles represent cells, and gels are not shown. (b–c) Phase diagrams showing the dependence of S on adhesion strength ($\hat{\epsilon}$), motility strength ($\hat{\Gamma}$), and packing fraction (ϕ_c) for a 2D system at $\hat{k}_a = 1$ and $E_g/E_c = 1$. (b) shows a $\hat{\Gamma} - \hat{\epsilon}$ plane at $\phi_c = 0.3$ and (c) shows a $\hat{\Gamma} - \phi_c$ plane at $\hat{\epsilon} = 0.3$. (d–g) Variation of S with individual parameters: (d) S vs. $\hat{\epsilon}$ at $\phi_c = 0.3$ for different $\hat{\Gamma}$; (e) S vs. ϕ_c at $\hat{\epsilon} = 0.3$ for different $\hat{\Gamma}$; (f) S vs. $\hat{\Gamma}$ at $\phi_c = 0.3$ for different $\hat{\epsilon}$; (g) S vs. $\hat{\Gamma}$ at $\hat{\epsilon} = 0.3$ for different ϕ_c.

noise, and $\hat{\Gamma}$ represents the strength of cellular motility. Following the properties of an Ornstein-Uhlenbeck process, the time correlation of the force evolves as,

$$\langle \vec{\hat{F}}_i^{\mathrm{A}}(0) \cdot \vec{\hat{F}}_i^{\mathrm{A}}(\hat{t}) \rangle = \frac{d\hat{\Gamma}^2}{\hat{k}_a} e^{(-\hat{k}_a \hat{t})} \delta_{ij}, \tag{7}$$

where, d is the dimension of the simulation box.

Altogether, we explore the effects of the following parameters in our simulation: $\frac{E_g}{E_c}$ (relative stiffness of the background medium and the cells), $\hat{\epsilon}$ (the strength of adhesion), $\hat{k}_a$ (inverse persistence timescale), $\hat{\Gamma}$ (the strength of motility), and ϕ_c (packing fraction of the cells). In this study we use a densely packed box, where the volume of undeformed cells and gels are equal to the volume of the box (i.e. $\phi_c + \phi_g = 1$, where ϕ_g is the volume fraction of the gels). Specifically, we create a non-overlapping configuration of cells using Random Sequential Addition (RSA) and fill the rest of the space with gels, which may overlap with each other but don't overlap with the cells.

III. RESULTS AND DISCUSSIONS

In this section of the manuscript, we examine how the physical parameters introduced above influence collective cell self-assembly, specifically focusing on the formation of multicellular clusters, as well as the dynamics of individual cells.

A. Quantifying and mapping the degree of self-assembly

To quantify the degree of self-assembly, we identify clusters of connected cells. Two cells are defined as connected if their separation is less than a cutoff radius $r_c = (1 + \delta)\sigma$, where δ is the non-dimesionalized half-width of the range of the attractive potential [Fig. 1(a)] and σ is the cell diameter. Based on this criterion, we construct an adjacency matrix and determine the number of independent clusters, N_{conn}. We define the order parameter $S = N_{\mathrm{conn}}/N_{\mathrm{cell}}$, where, N_{cell} is the total number of cells [Fig. 2(a)]. S measures the degree of self-assembly. $S = 1$ corresponds to fully isolated cells, while $S = 1/N_{\mathrm{cell}} \approx 0$ corresponds to a single connected cluster. Thus, lower S indicates stronger self-assembly.

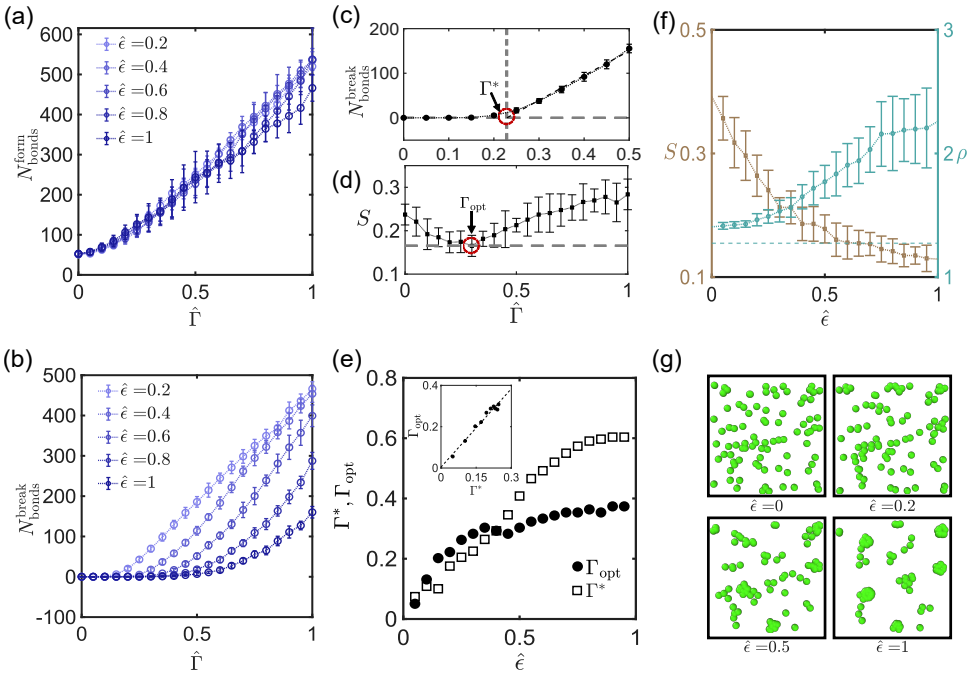

FIG. 3. (a-b) Number of bonds (cell-cell adhesion) formed (a) and broken (b) as a function of motility strength $\hat{\Gamma}$ for different adhesion strengths $\hat{\epsilon}$. (c) Definition of Γ^*, the minimum motility required to break intercellular bonds. (d) Definition of $\Gamma_{\rm opt}$, the motility level at which self-assembly is maximium (S is minimum). (e) Variation of Γ and $\Gamma_{\rm opt}$ on $\hat{\epsilon}$. The inset shows a scatter plot of Γ^* versus $\Gamma_{\rm opt}$ for $0 < \hat{\epsilon} < 0.5$; the dashed line indicates a linear fit with slope m = 1.26. (f) Order parameter S (left axis) and local number density ρ (right axis) as functions of $\hat{\epsilon}$. The dotted line represents number density of an isolated cell (i.e.$4/\pi$). (g) Representative simulation snapshots showing cells (green) at $\hat{\epsilon} = \{0, 0.2, 0.5, 1\}$ for $\hat{\Gamma} = 0.5$ and $\phi_{\rm c} = 0.3$. Gel particles are not shown.

We begin our exploration of phase-space by systematically varying the motility strength ($\hat{\Gamma}$), adhesion strength ($\hat{\epsilon}$), and packing fraction ($\phi_{\rm c}$) for two-dimensional simulations keeping $\hat{k}_{\rm a} = 1$ and $E_g/E_c = 1$. Figures 2(b–c) show the dependence of S on these parameters in the $\hat{\Gamma}$–$\hat{\epsilon}$ and $\phi_{\rm c}$–$\hat{\Gamma}$ planes. As expected, S decreases (indicating stronger self-assembly) with increasing adhesion strength $\hat{\epsilon}$ [Fig. 2(d)] and with increasing packing fraction $\phi_{\rm c}$ [Fig. 2(e)].

In contrast, the dependence of S on motility strength $\hat{\Gamma}$ is non-monotonic. At small $\hat{\Gamma}$, increasing motility enhances self-assembly (decreasing S), whereas at large $\hat{\Gamma}$, excessive motility disrupts clusters (increasing S) [Fig. 2(f)]. Moreover, S increases with $\hat{\Gamma}$ at higher densities of cells and decreases with $\hat{\Gamma}$ at lower densities of cells [Fig. 2(g)]. Thus, motility exerts a dual effect—it can either promote or hinder self-assembly depending on the parameter regime. Similar effect of motility in self-assembly is also observed in other active matter systems as well [29, 53].

The qualitative dependence of S on the three parameters are similar in three dimensions as well (Supplementary Fig. S1, Supplementary Movie 1). So, the remainder of our analysis focuses on two-dimensional systems for ease of computation.

B. Interaction of motility and adhesion in cellular self-assembly

Next, we investigate what leads to this two-way effect of motility in self-assembly and what sets the optimum motility for self-assembly. We observe the dynamics of self-assembly (Supplementary Movie 2) for the simulations with same strength of adhesion and packing densities of cells but for different strength of motility. When cells are non-motile (i.e. $\hat{\Gamma} = 0$), cells just locally rearrange and no specific self-assembly happens. At intermediate motility, cells can explore the simulation domain and encounter one another and adhere to each other, promoting formation of assembled structures. However, in the higher level of $\hat{\Gamma}$, although the self-assembly happens the cells are too motile and the assembled structures become unstable.

To disentangle the two competing roles of motility in self-assembly, we quantify the number of adhesive bonds formed and broken in each simulation, defining two cells as bonded if their separation is below $r_{\rm c}$. Both quantities increase with $\hat{\Gamma}$, consistent with the observed two-way behavior of motility [Fig. 3(a–b)]. However, they do so in fundamentally different ways: the number of bonds formed grows steadily with increasing $\hat{\Gamma}$, whereas the number of broken bonds remains negligible until a threshold motility Γ^* is reached, after which it rises sharply. We

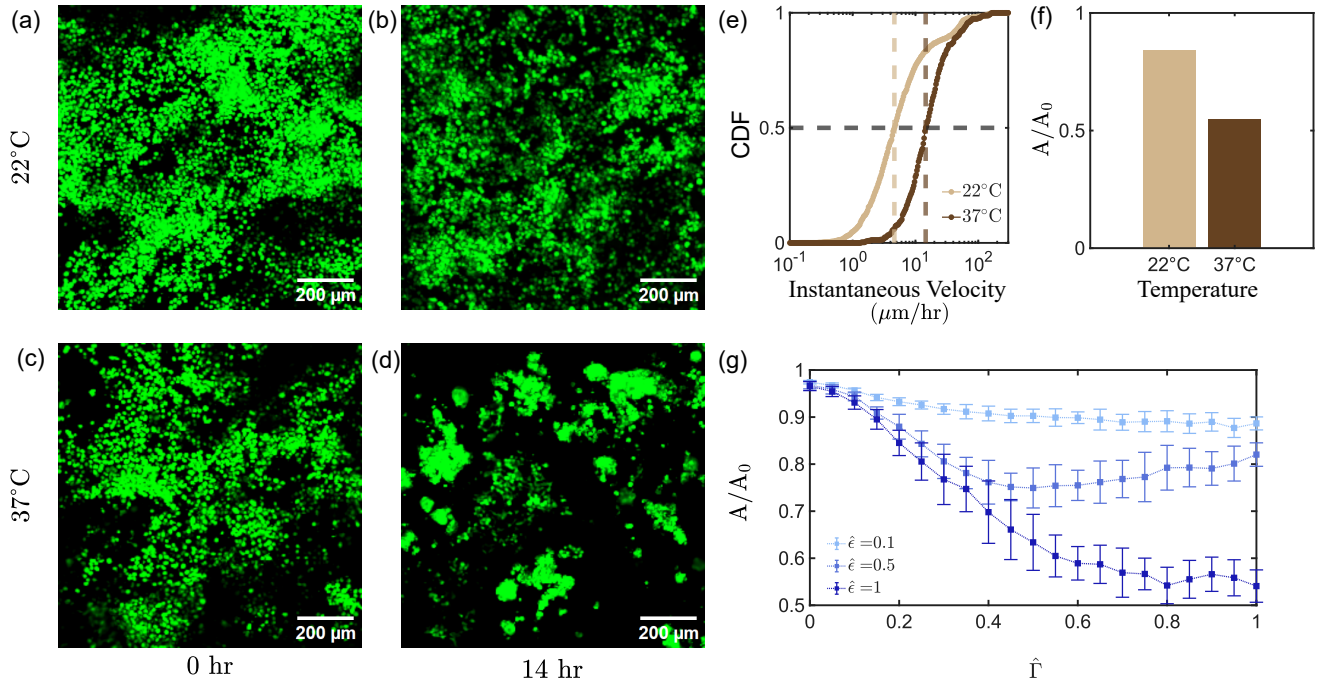

FIG. 4. (a-d) Maximum intensity projections from micrographs of fluorescently-labelled MCF7 cells dispersed in a microgel matrix, captured at both 0 hour and post 14-hour timepoints, across both (a and b) low (22°C) and (c and d) high (37°C) temperatures. Scalebars denote 200 μm. (e) Cumulative distribution of all instantaneous speeds recorded for individual cells over four hours of timelapse imaging across both low (22°C) and high (37°C) temperatures. The horizontal dotted line represents CDF=0.5 and the verticle dotted line represents the median speed for the respective temperatures. (f) Quantification of area fractions occupied by MCF7 cells and clusters from max-projected confocal micrographs, represented as 14-hour timepoint values normalized against the 0-hour timepoint values. (g) Ratio of area occupied by the cells at the beginning and end of the simulation as a function of $\hat{\Gamma}$ for varying $\hat{\epsilon}$ for simulations done with $\phi_c = 0.3$, $\hat{k_a} = 1$ and $E_g/E_c = 1$.

therefore define Γ^* as the minimum motility required to disrupt an adhesive cell–cell bond [Fig. 3(c)]. We further define an optimal motility $\Gamma_{\rm opt}$ as the value of $\hat{\Gamma}$ that minimizes S for a given $\hat{\epsilon}$ [Fig. 3(d)], and hypothesize that Γ^* and $\Gamma_{\rm opt}$ should be related. Indeed, both increase with adhesion strength $\hat{\epsilon}$, but their behaviors diverge at larger values of $\hat{\epsilon}$ [Fig. 3(e)]. For $\hat{\epsilon} \leq 0.5$, Γ^* and $\Gamma_{\rm opt}$ remain linearly correlated, as shown in the inset of Fig. 3(e). Beyond this regime, $\Gamma_{\rm opt}$ saturates while Γ^* continues to increase, indicating that additional motility continues to break bonds but no longer alters the number of connected clusters. This is consistent with the plateau in S observed for $\hat{\epsilon} > 0.5$ [Fig. 3(f)].

Why is additional motility required to break the bonds for $\hat{\epsilon} > 0.5$ while there is no change in the number of cells in the cluster? We examine the simulation snapshots at fixed $\hat{\Gamma}$ and varying $\hat{\epsilon}$. The number of clusters decreases with $\hat{\epsilon}$ up to ~ 0.5 and remains constant thereafter, while the clusters become increasingly compact [Fig. 3(g)]. To quantify the compactness, we calculate the average local packing fraction of individual clusters weighted by the number of cells in each cluster as,

$$\rho = \frac{1}{\sum N_i} \sum \frac{N_i^2}{A_i}, \tag{8}$$

where , N_i is the number of cells in a cluster and A_i is the total area occupied by the cluster [Supplementary Fig. S2(a-b)]. At low values of $\hat{\epsilon}$, the packing fraction ρ remains close to that of an isolated sphere and exhibits only a weak dependence on $\hat{\epsilon}$. In contrast, for higher $\hat{\epsilon}$, ρ increases significantly, suggesting that the clusters transition to a more compact state with substantial cell–cell overlap [Fig. 3(f), Supplementary Fig. S2(c)].

Altogether, these results suggest that our simulations show the self-assembly of cells in two regimes. For $\hat{\epsilon} \lesssim 0.5$, increasing adhesion primarily increases cluster size, while for $\hat{\epsilon} > 0.5$, it primarily increases cluster compactness. This crossover arises from the balance between adhesion and repulsion. Formation of compact clusters requires partial overlap, which incurs a repulsive energy cost. As shown in Fig. 1(c), the characteristic repulsive force magnitude is fixed at 0.5 in our non-dimensional units. When $\hat{\epsilon} \geq 0.5$, adhesion becomes comparable to (or stronger than) repulsion, enabling cells to overlap and form more and more compact assemblies.

C. Quantifying the effect of motility in *in vitro* cell culture experiment

Next, we asked whether the simulation-based predictions are consistent with the aggregation behavior of real

cells in a viscoelastic environment. A previous study [12] reported that cells form clusters whose extent increases with both cell density and intercellular adhesion, controlled by E-cadherin overexpression. This trend closely parallels our simulation results. We designed a similar experimental assay, but instead of modulating adhesion, we tuned the strength of cellular motility. Specifically, we culture a breast cancer cell line (MCF7) in non-adherent condition in a granular and porous viscoelastic 3D cell growth media comprising jammed packings of agarose granules generated using a flash solidification strategy [54](Supplementary methods). Prior characterizations of such microgels have reported individual particle sizes as 100 ± 40 μm, whereas, the interparticle pore spaces range from 1-20 μm suggesting a packed microgel medium similar to our simulation. Rheological measurements confirmed that microgel medium is viscoelastic, with storage modulus exceeding loss modulus on relevant timescales, and that it exhibits yield-stress behavior (Supplementary methods, Supplementary Fig. S3).

To modulate motility, we cultured cells at two temperatures: 22°C and 37°C with atmospheric CO_2 concentration controlled at 5% for both conditions. Using timelapse imaging (Supplementary methods, Supplementary Movie 3), we tracked motion with single cell resolution in 3D. The instantaneous speed distribution shifted to higher values at 37°C. Specifically, a Kolmogorov-Smirnovtest shows that the distributions are significantly different with p value < 0.0001 and the median speed changes from 4.62 μm/hr to 14.54 μm/hr [Fig. 4(e)]. We note that the speed of an isolated cell in our model corresponds to the parameter $\hat{\Gamma}^2/2\hat{k}_{\rm a}$, directly linking experimental results to the model parameters.

How does motility influence the self-organized clustering of these cancer cells? Over a 14-hour experiment, slower motion aberrantly affects self-organized aggregation. While MCF7 cells maintained under 22°C remain largely dispersed, cells maintained under 37°C collectively organize into aggregates [Fig. 4(a)–(d), Supplementary methods]. Although the imaging resolution prevents segmentation of individual cells—and thus we cannot compute the metric S, we quantified the total area occupied by cells at the beginning and end of the experiment [Fig. 4(f)]. In both conditions, the occupied area decreases over time. This reduction is significantly greater at 37°C, demonstrating that stronger motility enhances self-assembly *in vitro*.

To directly compare the experimental results to simulation predictions, we evaluate the ratio of the final to initial occupied area as:

$$\frac{A}{A_0} = \frac{\sum_{i\in C} A_i,}{L^2\phi_{\rm c}}, \tag{9}$$

where, A_i are the areas of the individual clusters as introduced in Eq. 8, L is the box length, and $\phi_{\rm c}$ is cell volume fraction. The initial area is computed as $L^2\phi_{\rm c}$ as we start from a configuration with non-overlapping cells. In simulations, A/A_0 varies weakly with $\hat{\Gamma}$ at low $\hat{\epsilon}$, becomes non-monotonic at intermediate $\hat{\epsilon}$, and decreases sharply at high $\hat{\epsilon}$ [Fig. 4(g)]. We emphasize that A/A_0 and S capture different aspects of organization: S decreases when the number of cells in an individual cluster increases, whereas A/A_0 decreases primarily when clusters become compact, which occurs only at higher $\hat{\epsilon}$ as observed in Fig. 3(f),(g). Furthermore, the indistinguishability of individual cells inside the clusters are also consistent with the high-$\hat{\epsilon}$ regime of our phase diagram, where we observe strong overlap and compact aggregates. Altogether, the experiments capture a regime where motility enhances self-assembly without becoming strong enough to disrupt the formed clusters, a behavior that does not appear in systems at equilibrium.

D. Effect of persistence time on self-assembly

We next examine how the persistence timescale of motility, defined as $1/\hat{k}_{\rm a}$, influences cellular self-assembly. To this end, we compute the order parameter S as a function of $\hat{\Gamma}$ and $\hat{k}_{\rm a}$ while keeping $\hat{\epsilon} = 0.5$ and $\phi_{\rm c} = 0.3$ fixed. We find that S exhibits a non-monotonic dependence on $\hat{k}_{\rm a}$, with the minimum shifting to higher $\hat{k}_{\rm a}$ values as $\hat{\Gamma}$ increases [Fig. 5(a)–(c)]. Remarkably, all data collapse onto a single non-monotonic curve when the x-axis is rescaled as $\hat{\Gamma}^2/\hat{k}_{\rm a}$ [Fig. 5(d)].

This rescaling has a clear physical interpretation. From Eq. 7, the zero-time value of the force–force autocorrelation function that represents the mean squared magni-

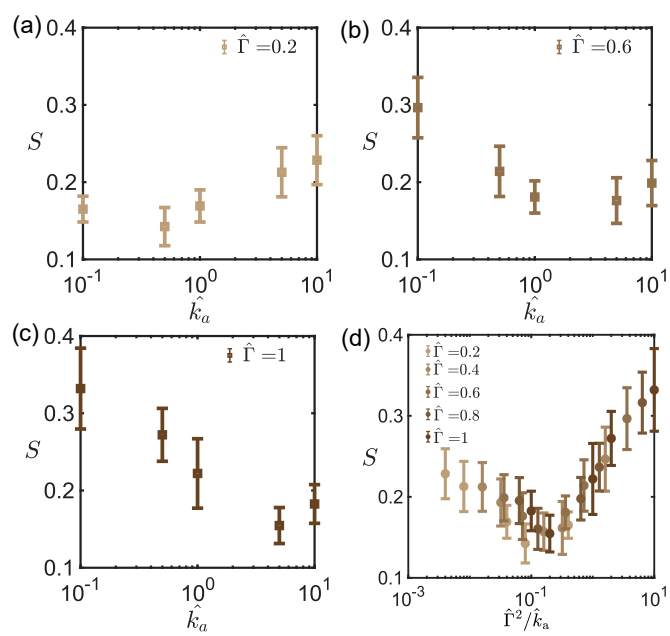

FIG. 5. (a-c) S as a function of the inverse persistence time of motility ($\hat{k}_{\rm a}$) for different strengths of motility ($\hat{\Gamma} = 0.2, 0.4, 1$), respectively for $\hat{\epsilon} = 0.5$ and $\phi_c = 0.3$. (d) S plotted against $\hat{\Gamma}^2/\hat{k}_{\rm a}$ for different $\hat{\Gamma}$ at the same $\hat{\epsilon}$ and $\phi_{\rm c}$.

tude of the active force, is proportional to $\hat{\Gamma}^2/\hat{k}_\mathrm{a}$. Therefore, the degree of self-assembly is primarily governed by the characteristic magnitude of the self-propulsion force. While the temporal decay of the autocorrelation does not directly control self-assembly, it influences it indirectly by modulating the effective strength of motility.

E. Effect of medium stiffness on self-assembly

In the preceding results, the background medium (gel) was assumed to have the same stiffness as the cells. We now relax this constraint to evaluate how gel stiffness influences self-assembly. We compute the order parameter S by varying $\hat{\Gamma}$ and the stiffness ratio E_g/E_c, while keeping $\hat{k}_\mathrm{a} = 1$, $\hat{\epsilon} = 0.5$, and $\phi_\mathrm{c} = 0.3$ fixed. We find that background stiffness significantly affects self-assembly when motility is weak. At small or zero $\hat{\Gamma}$, stiffer gels promote self-assembly of cells even in absence of any adhesive force ($\hat{\epsilon} = 0$) [Fig. 6(a)]. The effect persists in presence of adhesion ($\hat{\epsilon} > 0$). However, for $\hat{\Gamma} > 0$, the effect of background stiffness becomes negligible (Supplementary Fig. S4).

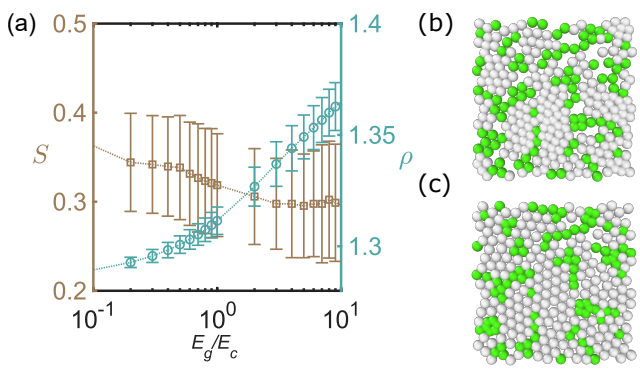

FIG. 6. (a) S and ρ as a function of the E_g/E_c for motility strength ($\hat{\Gamma}$=0) at $\hat{k}_\mathrm{a} = 1$, $\hat{\epsilon} = 0$ and $\phi_\mathrm{c} = 0.3$. (b-c) Snapshot of cellular assembly for non-motile cells (green) dispersed within gels (grey) with relative stiffness $E_g/E_c = 0.1$, and $E_g/E_c = 10$ respectively for the same simulations.

To understand this behavior, we analyze simulations with zero motility ($\hat{\Gamma} = 0$). When the gel is soft ($E_g/E_c = 0.1$), cells undergo almost no rearrangement, leading to minimal self-assembly [Fig. 6(b), Supplementary Movie 4]. In contrast, when the gel is much stiffer than the cells ($E_g/E_c = 10$), the strong repulsive forces within the gel drive it to eliminate overlap. This compaction effectively pushes cells together even at the energy cost of their overlap promoting cluster formation even without motility [Fig. 6(c), Supplementary Movie 4]. This is also evident from the increasing compactness of the cluster [Fig. 6(a)]. Once motility is present, however, cells can explore space and locate neighbors autonomously, making this gel-induced "mechanical push" redundant for assembly of cells.

F. Effect of cell-cell adhesion and background stiffness in cell dynamics

Finally, we investigate the effect of different physical parameters on cell dynamics by computing the mean squared displacement (MSD) of the cells. The primary determinant of the dynamics are the strength ($\hat{\Gamma}$) and persistence (represented by $\hat{k}_\mathrm{a}^{-1}$) of motility. In fact, in absence of any interaction force, the MSD of an isolated cell are only dependent on these two parameters, and can be computed analytically from Eq. 7 as,

$$\mathrm{MSD} = 4\hat{D}_a\sigma^2\left[\hat{t} + \frac{1-\exp(-\hat{k}_a\hat{t})}{\hat{k}_a}\right], \qquad (10)$$

where, $\hat{D}_\mathrm{a} = \hat{\Gamma}^2/2\hat{k}_\mathrm{a}^2$ is an effective long-time diffusivity resulting from the self-propulsion, and σ is the cell diameter [Fig. 7 (a)]. This shows a ballistic behavior at

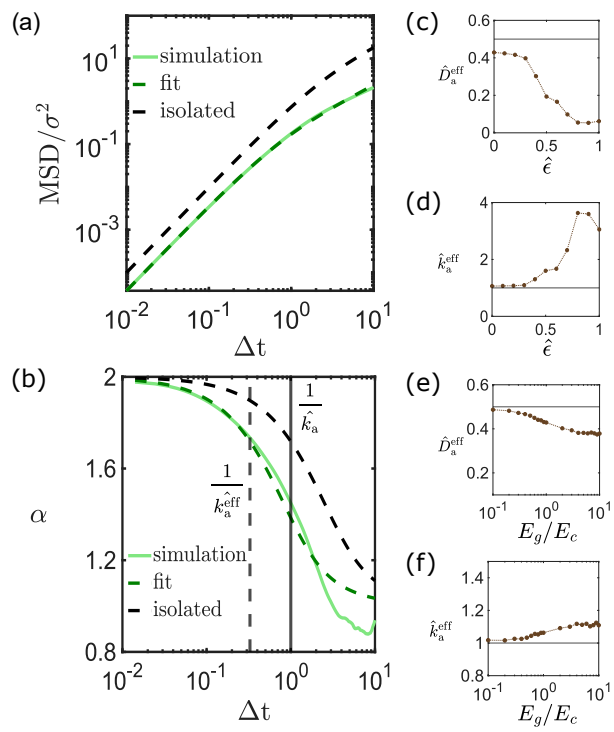

FIG. 7. (a) Mean squared displacement (MSD) vs time plots for an isolated cell (derived analytically), from simulation and the fitted MSD with same analytical expressions with parameters ($\hat{D}_\mathrm{a}^\mathrm{eff}$ and $\hat{k}_\mathrm{a}^\mathrm{eff}$). (b) The time exponent of MSD ($\alpha = \frac{\mathrm{d}\ln(\mathrm{MSD})}{\mathrm{d}\ln(t)}$) for the same three cases. The solid and dashed line in (b) represent the characteristic timescales of superdiffusive to diffusive transition for the isolated cell and the cells in the simulation, $1/\hat{k}_\mathrm{a}$, and $1/\hat{k}_\mathrm{a}^\mathrm{eff}$, respectively. (c-d) The effective parameters $\hat{D}_\mathrm{a}^\mathrm{eff}$ and $\hat{k}_\mathrm{a}^\mathrm{eff}$ as a function of $\hat{\epsilon}$ for $E_g/E_c = 1$, $\hat{\Gamma} = 1$, and $\hat{k}_\mathrm{a} = 1$, respectively. (e-f) The effective parameters $\hat{D}_\mathrm{a}^\mathrm{eff}$ and $\hat{k}_\mathrm{a}^\mathrm{eff}$ as a function of E_g/E_c for $\hat{\epsilon} = 0$, $\hat{\Gamma} = 1$, and $\hat{k}_\mathrm{a} = 1$. The dotted lines represent $\hat{D}_\mathrm{a}$ and $\hat{k}_\mathrm{a}$ for an isolated cell propelling with $\hat{\Gamma} = 1$, and $\hat{k}_\mathrm{a} = 1$.

short timescale (MSD $\propto \hat{t}^2$) and diffusive behavior at long timescale (MSD $\propto \hat{t}$), evident from the dynamics of the time exponent of MSD, $\alpha = \frac{\mathrm{d}\ln(\mathrm{MSD})}{\mathrm{d}\ln(t)}$ [Fig. 7 (b)]. The transition happens at the timescale of persistence of the self-propulsion force $\hat{k_{\mathrm{a}}}^{-1}$.

How does this behavior change in presence of interaction with other cells and the background gels? Although the MSD reduces, we can still fit it with Eq. 10 with a modified diffusivity $\hat{D}_{\mathrm{a}}^{\mathrm{eff}}$ and inverse persistence timescale $\hat{k}_{\mathrm{a}}^{\mathrm{eff}}$ [Fig. 7(a)-(b), Supplementary Fig. S5]. Both quantities depend strongly on adhesion: $\hat{D}\mathrm{a}^{\mathrm{eff}}$ decreases and $\hat{k}_{\mathrm{a}}^{\mathrm{eff}}$ increases progressively with $\hat{\epsilon}$ [Fig. 7(c)–(d)]. Even when adhesion is absent, $\hat{D}_{\mathrm{a}}^{\mathrm{eff}}$ and $\hat{k}_{\mathrm{a}}^{\mathrm{eff}}$ deviate from the isolated-cell prediction, suggesting an influence from the surrounding gel. To test this, we vary the background stiffness E_g/E_c while setting $\hat{\epsilon} = 0$. We find that stiffer gels further reduce $\hat{D}_{\mathrm{a}}^{\mathrm{eff}}$ and increase $\hat{k}_{\mathrm{a}}^{\mathrm{eff}}$ [Fig. 7(e)–(f)].

Altogether, these observations suggest that presence of cell-cell adhesion as well as the interaction with the background gels reduces the net displacement as well as the persistence timescale of the cells. Physically, adhesion promotes the formation of multicellular aggregates. These assemblies are larger entities than individual cells and comprise many cells whose self-propulsion vectors are oriented in different directions, leading to partial cancellation of active forces. Consequently, both the net displacement and the effective persistence of motion are reduced relative to isolated cells. Similarly, a stiffer background gel increases mechanical resistance, making it harder for cells to migrate resulting into loss of persistence as well as overall displacement.

IV. CONCLUSIONS

In this article, we present an agent-based computational framework, where cells are represented as soft self-propelling particles adhering to each other submerged in a passive viscoelastic environment (Fig. 1). We utilize this framework to study how the density, strength of adhesion, strength of motility, persistence time, and relative stiffness with the background determines the self-assembly of cell (Fig. 2, 5, 6). We specifically focus on the interplay of adhesion and motility in the self-assembly (Fig. 3). Further, we experimentally validate our predictions using self-aggregating cancer cells cultured in a granular microgel matrix, and discover a behavior consistent with the high-adhesion region of the phase diagram (Fig. 4). Finally, we show that the adhesive interaction with other cells and contact interaction with the background medium reduce both the strength and persistence of the motiliy of the cells (Fig. 7).

Our simulations make several interesting predictions. First, they reveal a two-way role of motility in self-assembly. Motile cells are able to locate and join neighboring cells, but the same motion can also disrupt clusters that have already formed leading to a dynamic balance between assembly and disassembly. Although in our simulations, cells are motile and form clusters of higher local density, this phenomenon is not an example of motility-induced phase separation. Instead, it is a *motility-assisted* phase separation, because we observe negligible assembly when cells lack adhesive interactions in spite of motility. Adhesion also plays a two-stage role. At lower adhesion strengths, cells form stable multicellular structures, whereas stronger adhesion leads to progressively more compact clusters. This behavior arises from the competition between adhesive and repulsive forces and is a direct consequence of the choice of our force-field. Such effects would not be expected with a force-field inspired by molecular interactions (e.g. Lennard-Jones potential), where the strength of attraction and repulsion are intrinsically linked. In contrast, our force-field decouples these interactions, reflecting the biological reality that repulsion and adhesion originate from distinct mechanisms i.e., mechanical stiffness and E-cadherin–mediated binding, respectively.

We show that our simulation is qualitatively consistent with *in vitro* cell culture experiments from earlier reported results as well as new results reported here. Moreover, we would like to note that all the physical parameter are independent in our model. However, in reality they are often coupled. For example, cell migration is often modulated by the mechanical properties of the background. In future, a dedicated experimental work is needed to construct an experimental twin of the phase diagram we present in this manuscript, which will set the basis for an iterative process to reflect the coupling between the physical parameters in our model. We also note that, in this study, we only focus on the self-assembly of cells initially dispersed at random. The same framework, however, can be extended to simulate the evolution of preassembled tissues in soft background, such as those generated by 3D bioprinting [55, 56]. Specifically, the model could serve as a platform for designing tissues with switchable morphologies by tuning biophysical parameters. Thus, the framework not only provides insight into how physical interactions shape cellular self-assembly, but also lays the groundwork for the integrated design of engineered tissues that are indeed printable in soft environments.

ACKNOWLEDGMENTS

S. Das acknowledges IIT Bombay graduate fellowship. M.S. acknowledges TIFR graduate fellowship. We acknowledge Prof. Aravind Ramanathan for generously sharing the MCF7 cells. We thank Rujula Jagadeesh for assistance with the 3D microgel preparation and characterization. S. Dutta and T.B. acknowledge funds received from Department of Biotechnology, Govt. of India vide grant no BT/PR54128/BMS/85/596/2024. S. Dutta also acknowledges seed grant from IIT Bombay vide project RD/0523-IRCCSH0-022.

DATA AVAILABILITY STATEMENT

The simulation software, the simulation data, and experimental images will be available on reasonable request to the corresponding authors.

AUTHOR CONTRIBUTIONS

S. Dutta and T.B. conceptualized the project and acquired funding. S.Das, D.P., and S. Dutta developed the simulation software. S. Das ran the simulations. S. Das and S. Dutta analyzed the simulation results. M.S. conducted the cell culture and imaging experiments and analyzed the imaging data. S. Das visualized the data. S. Dutta, S. Das, and M.S. prepared the manuscript. All the authors reviewed the manuscript.

SUPPLEMENTARY MATERIAL

A supplementary material file is attached with a supplementary note on the experimental methods and supplementary figures 1-5. Supplementary movies 1-4 are also attached seperately. References [54, 57–60] are referred to in the supplementary note.

[1] Maria Leptin. *Drosophila* gastrulation: from pattern formation to morphogenesis. *Annual review of cell and developmental biology*, 11:189–212, 1995.

[2] Hiroshi Koyama, Hisashi Okumura, Atsushi M Ito, Kazuyuki Nakamura, Tetsuhisa Otani, Kagayaki Kato, and Toshihiko Fujimori. Effective mechanical potential of cell–cell interaction explains three-dimensional morphologies during early embryogenesis. *PLoS Computational Biology*, 19(8):e1011306, 2023.

[3] Kim S Midwood, Leyla Valenick Williams, and Jean E Schwarzbauer. Tissue repair and the dynamics of the extracellular matrix. *The international journal of biochemistry & cell biology*, 36(6):1031–1037, 2004.

[4] Kenechukwu David Nnetu, Melanie Knorr, Dan Strehle, Mareike Zink, and Josef A Käs. Directed persistent motion maintains sheet integrity during multi-cellular spreading and migration. *Soft Matter*, 8(26):6913–6921, 2012.

[5] Laurence Petitjean, Myriam Reffay, Erwan Grasland-Mongrain, Mathieu Poujade, Benoıt Ladoux, Axel Buguin, and Pascal Silberzan. Velocity fields in a collectively migrating epithelium. *Biophysical journal*, 98 (9):1790–1800, 2010.

[6] Sorinel Adrian Oprisan, Aurel Ardelean, and Petre T Frangopol. Self-organization and competition in the immune response to cancer invasion: a phase-orientated computational model of oncogenesis. *Bioinformatics*, 16 (2):96–100, 2000.

[7] Jun Yokota. Tumor progression and metastasis. *Carcinogenesis*, 21(3):497–503, 2000.

[8] Nareg J-V Djabrayan, Celia M Smits, Matej Krajnc, Tomer Stern, Shigehiro Yamada, William C Lemon, Philipp J Keller, Christine A Rushlow, and Stanislav Y Shvartsman. Metabolic regulation of developmental cell cycles and zygotic transcription. *Current Biology*, 29(7): 1193–1198, 2019.

[9] Celia M Smits, Sayantan Dutta, Vishank Jain-Sharma, Sebastian J Streichan, and Stanislav Y Shvartsman. Maintaining symmetry during body axis elongation. *Current Biology*, 33(16):3536–3543, 2023.

[10] Jonathan A Brassard and Matthias P Lutolf. Engineering stem cell self-organization to build better organoids. *Cell stem cell*, 24(6):860–876, 2019.

[11] B Ladoux, WJ Nelson, J Yan, and RM Mège. The mechanotransduction machinery at work at adherens junctions. *Integrative Biology*, 7(10):1109–1119, 2015.

[12] Cameron D Morley, Jesse Tordoff, Christopher S O'Bryan, Ron Weiss, and Thomas E Angelini. 3d aggregation of cells in packed microgel media. *Soft Matter*, 16(28):6572–6581, 2020.

[13] Sayantan Dutta, Nareg J-V Djabrayan, Salvatore Torquato, Stanislav Y Shvartsman, and Matej Krajnc. Self-similar dynamics of nuclear packing in the early *Drosophila* embryo. *Biophysical journal*, 117(4):743–750, 2019.

[14] James Giammona and Otger Campàs. Physical constraints on early blastomere packings. *PLoS Computational Biology*, 17(1):e1007994, 2021.

[15] Evanthia T Roussos, John S Condeelis, and Antonia Patsialou. Chemotaxis in cancer. *Nature Reviews Cancer*, 11(8):573–587, 2011.

[16] Chun-Min Lo, Hong-Bei Wang, Micah Dembo, and Yu-li Wang. Cell movement is guided by the rigidity of the substrate. *Biophysical journal*, 79(1):144–152, 2000.

[17] Shuvasree SenGupta, Carole A Parent, and James E Bear. The principles of directed cell migration. *Nature Reviews Molecular Cell Biology*, 22(8):529–547, 2021.

[18] EN Cytrynbaum and JM Scholey. A force balance model of early spindle pole separation in *Drosophila* embryos. *Biophysical journal*, 84(2):757–769, 2003.

[19] Torey R Arnold, Rachel E Stephenson, and Ann L Miller. Rho gtpases and actomyosin: Partners in regulating epithelial cell-cell junction structure and function. *Experimental cell research*, 358(1):20–30, 2017.

[20] Katja Röper. Integration of cell–cell adhesion and contractile actomyosin activity during morphogenesis. *Current topics in developmental biology*, 112:103–127, 2015.

[21] Clarence E Chan and David J Odde. Traction dynamics of filopodia on compliant substrates. *Science*, 322(5908): 1687–1691, 2008.

[22] Alberto Elosegui-Artola, Elsa Bazellières, Michael D Allen, Ion Andreu, Roger Oria, Raimon Sunyer, Jennifer J Gomm, John F Marshall, J Louise Jones, Xavier Trepat, et al. Rigidity sensing and adaptation through regulation of integrin types. *Nature materials*, 13(6):631–637, 2014.

[23] Sriram Ramaswamy. The mechanics and statistics of active matter. *Annu. Rev. Condens. Matter Phys.*, 1(1): 323–345, 2010.

[24] M Cristina Marchetti, Jean-François Joanny, Sriram Ramaswamy, Tanniemola B Liverpool, Jacques Prost, Madan Rao, and R Aditi Simha. Hydrodynamics of soft active matter. *Reviews of modern physics*, 85(3):1143–1189, 2013.

[25] Michael Te Vrugt and Raphael Wittkowski. Metareview: a survey of active matter reviews. *The European Physical Journal E*, 48(3):12, 2025.

[26] Michael E Cates and Julien Tailleur. Motility-induced phase separation. *Annu. Rev. Condens. Matter Phys.*, 6 (1):219–244, 2015.

[27] Jérémy O'Byrne, Alexandre Solon, Julien Tailleur, and Yongfeng Zhao. An introduction to motility-induced phase separation. 2023.

[28] David Selmeczi, Stephan Mosler, Peter H Hagedorn, Niels B Larsen, and Henrik Flyvbjerg. Cell motility as persistent random motion: theories from experiments. *Biophysical journal*, 89(2):912–931, 2005.

[29] Gabriel S Redner, Aparna Baskaran, and Michael F Hagan. Reentrant phase behavior in active colloids with attraction. *Physical Review E—Statistical, Nonlinear, and Soft Matter Physics*, 88(1):012305, 2013.

[30] Gabriel S Redner, Michael F Hagan, and Aparna Baskaran. Structure and dynamics of a phase-separating active colloidal fluid. *Biophysical Journal*, 104(2):640a, 2013.

[31] Tamás Vicsek, András Czirók, Eshel Ben-Jacob, Inon Cohen, and Ofer Shochet. Novel type of phase transition in a system of self-driven particles. *Physical review letters*, 75(6):1226, 1995.

[32] Isaac Theurkauff, Cécile Cottin-Bizonne, Jérémie Palacci, Christophe Ybert, and Lydric Bocquet. Dynamic clustering in active colloidal suspensions with chemical signaling. *Physical review letters*, 108(26): 268303, 2012.

[33] Ligesh Theeyancheri, Subhasish Chaki, Tapomoy Bhattacharjee, and Rajarshi Chakrabarti. Dynamic clustering of active rings. *Physical Review Research*, 6(1):L012038, 2024.

[34] Nitin Kumar, Harsh Soni, Sriram Ramaswamy, and AK Sood. Flocking at a distance in active granular matter. *Nature communications*, 5(1):4688, 2014.

[35] Mattia Scandolo, Johannes Pausch, and Michael E Cates. Active ising models of flocking: a field-theoretic approach. *The European Physical Journal E*, 46(10):103, 2023.

[36] John Toner and Yuhai Tu. Long-range order in a two-dimensional dynamical xy model: how birds fly together. *Physical review letters*, 75(23):4326, 1995.

[37] Anupam Gupta, Amal Roy, Arnab Saha, and Samriddhi Sankar Ray. Flocking of active particles in a turbulent flow. *Physical Review Fluids*, 5(5):052601, 2020.

[38] Snigdha Thakur and Raymond Kapral. Collective dynamics of self-propelled sphere-dimer motors. *Physical Review E—Statistical, Nonlinear, and Soft Matter Physics*, 85(2):026121, 2012.

[39] Dapeng Bi, Xingbo Yang, M Cristina Marchetti, and M Lisa Manning. Motility-driven glass and jamming transitions in biological tissues. *Physical Review X*, 6 (2):021011, 2016.

[40] Sébastien Michelin. Self-propulsion of chemically active droplets. *Annual Review of Fluid Mechanics*, 55(1):77–101, 2023.

[41] Wilton T Snead and Amy S Gladfelter. The control centers of biomolecular phase separation: how membrane surfaces, ptms, and active processes regulate condensation. *Molecular cell*, 76(2):295–305, 2019.

[42] Andreas Deutsch, Peter Friedl, Luigi Preziosi, and Guy Theraulaz. Multi-scale analysis and modelling of collective migration in biological systems, 2020.

[43] Tamás Vicsek and Anna Zafeiris. Collective motion. *Physics reports*, 517(3-4):71–140, 2012.

[44] Balint Szabo, GJ Szöllösi, B Gönci, Zs Jurányi, David Selmeczi, and Tamás Vicsek. Phase transition in the collective migration of tissue cells: experiment and model. *Physical Review E—Statistical, Nonlinear, and Soft Matter Physics*, 74(6):061908, 2006.

[45] Vincent Hakim and Pascal Silberzan. Collective cell migration: a physics perspective. *Reports on Progress in Physics*, 80(7):076601, 2017.

[46] Xavier Trepat and Erik Sahai. Mesoscale physical principles of collective cell organization. *Nature Physics*, 14 (7):671–682, 2018.

[47] Heinrich Hertz. The contact of elastic solids. *J Reine Angew, Math*, 92:156–171, 1881.

[48] Lorenzo Rovigatti, Nicoletta Gnan, Andrea Ninarello, and Emanuela Zaccarelli. Connecting elasticity and effective interactions of neutral microgels: The validity of the hertzian model. *Macromolecules*, 52(13):4895–4906, 2019.

[49] Katarína Mendová, Martin Otáhal, Mitja Drab, and Matej Daniel. Size matters: rethinking hertz model interpretation for cell mechanics using afm. *International journal of molecular sciences*, 25(13):7186, 2024.

[50] Kenneth Langstreth Johnson. *Contact mechanics*. Cambridge university press, 1987.

[51] Francisco J Sevilla, Rosalío F Rodríguez, and Juan Ruben Gomez-Solano. Generalized ornstein-uhlenbeck model for active motion. *Physical Review E*, 100(3):032123, 2019.

[52] George E Uhlenbeck and Leonard S Ornstein. On the theory of the brownian motion. *Physical review*, 36(5): 823, 1930.

[53] Jie Su, Mengkai Feng, Yunfei Du, Huijun Jiang, and Zhonghuai Hou. Motility-induced phase separation is reentrant. *communications physics*, 6(1):58, 2023.

[54] M Sreepadmanabh, Meenakshi Ganesh, Ramray Bhat, and Tapomoy Bhattacharjee. Jammed microgel growth medium prepared by flash-solidification of agarose for 3D cell culture and 3d bioprinting. *Biomedical Materials*, 18 (4):045011, 2023.

[55] Tapomoy Bhattacharjee, Steven M Zehnder, Kyle G Rowe, Suhani Jain, Ryan M Nixon, W Gregory Sawyer, and Thomas E Angelini. Writing in the granular gel medium. *Science advances*, 1(8):e1500655, 2015.

[56] Tapomoy Bhattacharjee, Carmen J Gil, Samantha L Marshall, Juan M Urueña, Christopher S O'Bryan, Matt Carstens, Benjamin Keselowsky, Glyn D Palmer, Steve Ghivizzani, C Parker Gibbs, et al. Liquid-like solids support cells in 3d. *ACS Biomaterials Science & Engineering*, 2(10):1787–1795, 2016.

[57] M Sreepadmanabh, Ashitha B Arun, and Tapomoy Bhattacharjee. Design approaches for 3D cell culture and 3D bioprinting platforms. *Biophysics Reviews*, 5(2), 2024.

[58] M Sreepadmanabh, Meenakshi Ganesh, Pratibha Sanjenbam, Christina Kurzthaler, Deepa Agashe, and Tapomoy Bhattacharjee. Cell shape affects bacterial colony growth under physical confinement. *Nature communications*, 15 (1):9561, 2024.

[59] M Sreepadmanabh, Mridul Gautam, Nikita Bagade, Sunil Laxman, and Tapomoy Bhattacharjee. 3D confinement physically regulates cell cycle progression in budding yeast. *bioRxiv*, pages 2025–07, 2025.

[60] Saheli Dey, M Sreepadmanabh, Sayan Kundu, Ashitha B Arun, Sandhya P Koushika, Shashi Thutupalli, Duncan Hewitt, and Tapomoy Bhattacharjee. Physical confinement regulates transition in nematode motility. *bioRxiv*, pages 2025–01, 2025.